

# Evolution of surface morphology from Stranski–Krastanov growth mode to step-flow growth mode in InSbBi thin films

Chandima Kasun Edirisinghe<sup>1</sup>, Anuradha Wijesinghe<sup>1</sup>, Anjali Rathore<sup>1</sup>, Pradip Adhikari<sup>1</sup>,  
Christopher Rouleau<sup>2</sup>, Joon Sue Lee<sup>1,\*</sup>

<sup>1</sup>Department of Physics and Astronomy, University of Tennessee, Knoxville, TN 37996, USA

<sup>2</sup>Center for Nanophase Materials Sciences division, Oak Ridge National Laboratory, USA

\*Corresponding author e-mail: jslee@utk.edu

## Abstract

The incorporation of dilute concentrations of bismuth (Bi) into traditional III-V alloys leads to significant reduction in bandgap energy, making InSbBi is a promising candidate for long-wavelength infrared photodetection sensors due to its small bandgap (<0.17 eV). Furthermore, InSbBi could serve as a valuable platform for spin dynamics and quantum phenomena due to its strong spin-orbit coupling. Despite its potential, the material quality of InSbBi alloys lags behind that of conventional III-V semiconductors, primarily due to the substantial challenges associated with incorporating Bi into InSb and producing high-quality InSbBi with varying Bi compositions. In this study, we address these issues by developing a method for growing smooth InSbBi thin films with tunable Bi incorporation up to 1.81% by the dynamic adjustment of Sb flux and careful control of the interplay between growth temperature and Bi flux using molecular beam epitaxy. This work paves the path for high-quality InSbBi thin films for applications in photodetection, spintronics, and quantum technology.

## I. INTRODUCTION

In recent years, extensive research has focused on III-V semiconductor alloys due to their potential applications in near- and mid-infrared optoelectronic tools and devices. One example is InSb which has been extensively used in mid-infrared photodetectors<sup>1,2</sup>. However, its energy bandgap of 0.17 eV limits its ability to detect photons in the long wavelength infrared (LWIR) range<sup>1</sup>. Hence, several III-V ternary alloys such as InTlSb<sup>3,4</sup>, InAsBi<sup>5,6</sup>, InTlP<sup>7,8</sup>, and InTlAs<sup>9,10</sup> have been investigated as suitable candidates. Despite the encouraging results, further reduction of bandgap energy is necessary for high-performance detector operation<sup>11</sup>. InSb has the smallest bandgap in established III-V semiconductors<sup>12</sup>. By incorporating bismuth (Bi) into InSb, the ternary alloy InSbBi which has a band gap even lower than InSb can be formed<sup>13,14</sup>. Hence, InSbBi has become an attractive material system for LWIR applications, and recent studies have demonstrated that InSbBi epitaxy films grown by molecular beam epitaxy (MBE) on InSb substrate have demonstrated a reduction of 35 meV/%Bi at room temperature as the Bi incorporation increases from 0.6% to 2.4%<sup>1,13</sup>.

The addition of Bi enhances the spin-orbit splitting energy of III-V semiconductors<sup>15</sup>. This is primarily due to Bi's high atomic number and strong nuclear charge<sup>16-18</sup>. The strong spin-orbit splitting energy, particularly in InSbBi, will enhance the Landau g-factor by altering the energy levels and spin states of electrons<sup>19,20</sup>, which may provide exciting opportunities for advanced spintronics applications<sup>21</sup> and quantum phenomena such as topological superconductivity<sup>22-25</sup>.

Theoretical and experimental studies of a significant band gap reduction and bowing of spin orbit splitting energy in GaAsBi has been reported<sup>15,18,26-28</sup>. However, there remains a limitation in the experimental research on InSbBi, which can be attributed to significant challenges associated with synthesizing high-quality InSbBi samples<sup>1</sup>. Even among the limited studies available, results have often been contradictory; for instance, some researchers have reported contraction of the lattice after Bi incorporation into InSb<sup>11,29</sup>, while others<sup>13,14,30</sup> have demonstrated lattice expansion. Furthermore,

Rajpalke *et al.*<sup>13</sup> reported that the growth temperature must be lower than 225°C for Bi incorporation above 1%, whereas White *et al.*<sup>14</sup> achieved 1.9% even at a higher growth temperature of 300°C, highlighting a discrepancy in the relationship between Bi incorporation and growth temperature.

In this work, we present a platform that enables precise control over Bi incorporation in epitaxial InSbBi films by focusing on the evolution of the surface morphology from Stranski-Krastanov (SK) to step-flow growth modes while maintaining a smooth surface morphology without Bi droplets on the surface. This is achieved by careful flux control of antimony (Sb) and Indium (In) and the interplay between growth temperature and Bi flux. The findings of this study will contribute to the fundamental understanding of thin-film technology and offer a practical approach for growing smooth InSbBi films with tunable Bi incorporation, facilitating their integration into hybrid heterostructures for optoelectronic and quantum devices.

## II. EXPERIMENTAL

InSbBi thin films were grown on homoepitaxial InSb buffer layer on InSb(001) substrate using MBE. 1 cm × 1 cm sized InSb(001) substrates, Ga-bonded on tantalum substrate holders, were outgassed at a manipulator temperature of 350°C for 1 hour in an ultrahigh vacuum (UHV) chamber with a base pressure of low 10<sup>-10</sup> Torr. The substrates were transferred to an interconnected III-V MBE chamber, and the native oxide was thermally desorbed at a substrate temperature of 445°C in the presence of Sb<sub>2</sub> flux. Then, an InSb homoepitaxial layer of 100 nm was grown at 400°C. The resulting buffer layer exhibited a streaky (1 × 3) reflection high energy electron diffraction (RHEED) patterns, providing *in-situ* confirmation of the reconstructed InSb surface achieved under Sb-rich growth conditions<sup>31</sup>. Subsequently, InSbBi thin films of 300 nm were (FIG. 1(a)) with a systematic variation of growth parameters. Initially, the V/III flux ratio was varied by adjusting the Sb flux dynamically (changing the position of the Sb valved cracker to provide only the necessary amount of Sb flux to change the RHEED surface reconstruction from (4 × 2) to (1 × 3), keeping the In and Bi fluxes constant at 4.9×10<sup>-7</sup> Torr

and  $1.7 \times 10^{-8}$  Torr respectively. The V/III flux ratio must be maintained around unity to grow high-quality InSbBi thin films. A ratio above unity results in a  $(1 \times 3)$  surface reconstruction while a ratio below unity results in a  $(4 \times 2)$  surface reconstruction<sup>31</sup>. Following this, the Bi flux was systematically varied from  $1.2 \times 10^{-8}$  Torr to  $5.0 \times 10^{-8}$  Torr, with the V/III flux ratio maintained at unity and the growth temperature kept constant at 200°C. Finally, the growth temperature was varied while keeping the Bi flux constant at  $1.7 \times 10^{-8}$  Torr and the V/III flux ratio at unity. Growth temperatures were determined using a pyrometer down to 300°C. This enabled manipulator thermocouple readings to be estimated down to 200°C.

Crystal structures of InSbBi films were characterized by x-ray diffraction (XRD) using a Malvern Panalytical X'pert3 Materials Research Diffractometer with Cu- $\alpha$  radiation source ( $\lambda=1.54$  Å). The dynamical diffraction curves for calculating the Bi incorporation were done using the X'Pert Epitaxy software. The InBi lattice constant was chosen to be 6.686 Å with a zinc blende structure for these simulations<sup>32</sup>. A Poisson ratio of 0.3503 was used for simulations<sup>1,2</sup>. Surface morphology of the grown InSbBi films was characterized by atomic force microscopy (AFM) using a Cypher S AFM machine. Two measurements were carried out for each sample covering a wider area of  $10 \times 10$   $\mu\text{m}^2$  and a smaller area of  $1 \times 1$   $\mu\text{m}^2$ .

### **III. RESULTS AND DISCUSSION**

#### **A. Effect of V/III ratio for the growth of InSbBi thin films**

A V/III ratio larger than unity leads to accumulation of Bi droplets on the surface as Bi atoms are unable to incorporate substitutionally<sup>1</sup> as Bi-adsorbed InSb under Sb-rich conditions show energetically favored reconstructions stabilized by Sb, despite the existence of Bi atoms<sup>33,34</sup>. To examine the impact of the V/III ratio larger than unity, an InSb film was grown with a V/III ratio of 1.1 at a growth temperature of 200°C, with a Bi flux of  $1.7 \times 10^{-8}$  Torr. The resulting surface morphology shown in the AFM images in Fig. 1(b), reveals the formation of Bi droplets on the surface

(left panel). The magnified  $1 \times 1 \mu\text{m}^2$  area AFM scan in Fig. 1(b) right panel further highlights the formation of nanostructures oriented along the [110] direction likely formed by Bi.

To examine the effect of a flux ratio at unity, another InSb film was grown with a flux ratio of unity at a growth temperature of  $200^\circ\text{C}$ , with a Bi flux of  $1.7 \times 10^{-8}$  Torr. The resulting surface morphology exhibits a transition from nanostructures to mound formation, as shown in Fig. 1(c), indicating a shift in the growth mode. This morphological evolution will be further discussed in Sec. B: *Change in Structural Morphology with Varying Bi Flux*.

If the V/III ratio is less than unity, Bi incorporation will be suppressed despite the existence of Bi atoms on the growing surface. The strength of the In-Sb bond is considered to be stronger than that of In-Bi. Therefore, the Sb atoms are preferentially incorporated, while the Bi atoms encounter an increased difficulty to incorporate. Furthermore, the In-Bi bond is easily replaced by the In-Sb bond<sup>35</sup>. This will lead to having rough surfaces. To examine the impact of having a V/III ratio lesser than unity, a sample was grown with a V/III ratio of 0.9 at a growth temperature of  $200^\circ\text{C}$  with a Bi flux of  $1.7 \times 10^{-8}$  Torr, and the resulting surface morphology is shown in the AFM images in Fig. 1(d). Formation of droplets on the surface is visible as shown in Fig. 1(d) left panel. These droplets are likely to be In droplets since the film was grown under In-rich conditions. When zoomed in on the surface, step flow growth is visible as shown in Fig. 1(d) right panel. The step flow growth happens because of the growth of InSb {AFM images in Fig. 2(a)} without the incorporation of Bi into the grown film.

Wide area  $\theta/2\theta$  XRD scans were conducted to investigate the effect of the flux ratio, as shown in Fig. 1(e). In addition to the InSb(00n) substrate peaks, no other peaks corresponding to In or Bi are observed. This suggests that the Bi and In droplets, visible in Figs. 1(b) and (d) respectively, are not epitaxial. To further evaluate the impact of the flux ratio on Bi incorporation, small area  $\theta/2\theta$  XRD scans were performed, as illustrated in Fig. 1(f). A distinct peak corresponding to InSbBi is observed

when the flux ratio is at unity. However, no InSbBi peaks are detected when the V/III flux ratio is either greater than or less than unity (1.1 and 0.9), and no InSbBi peaks are observed when that V/III flux ratio is either greater than or lesser than unity (1.1 and 0.9). This demonstrates that the V/III ratio plays a critical role in the incorporation of Bi into InSb to form InSbBi thin films.

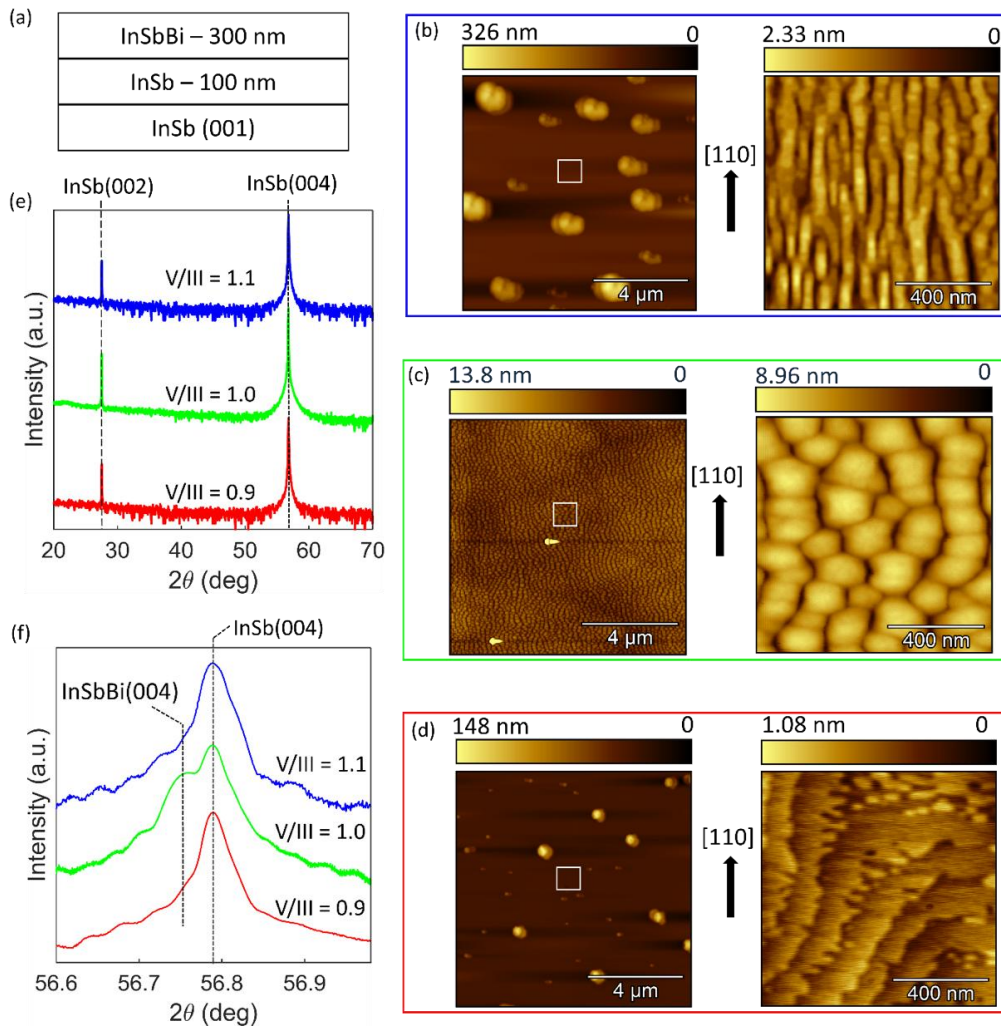


FIG. 1: Effect of V/III ratio on the InSbBi growth. (a) Structure of the samples. (b-d) AFM scans when the flux ratio is 1.1, 1.0, and 0.9, respectively. Left and right panels of (b-d) show surface areas of  $10 \times 10 \mu\text{m}^2$  and  $1 \times 1 \mu\text{m}^2$ , respectively. The magnified regions in the right panels correspond to the areas outlined by the white boxes in the left panels. The black arrow corresponds to the [110] direction of the AFM images. (e) Wide area  $\theta/2\theta$  XRD scans for the samples. (f) Small area  $\theta/2\theta$  XRD scans for the samples.

## **B. Change in surface morphology with varying Bi flux**

The change in the structural morphology of InSbBi films was studied systematically by varying the Bi flux up to  $5.0 \times 10^{-8}$  Torr, keeping the growth temperature constant at  $200^\circ\text{C}$ . The surface morphology changes as the Bi flux varies, as shown in AFM images in Fig. 2. InSb exhibits the morphology of step edges (Fig. 2(a)). With the introduction of Bi flux, the step edges of InSb vanish, following the nonequilibrium morphological evolution into “mound” structures as shown in Figs. 2(b) and 2(c). This morphological evolution occurs due to significant Ehrlich–Schwöebel barriers (also called step-edge barriers) that inhibit movement of atoms between layers of the growing interface<sup>36–38</sup>. Here, the onset of morphological instability does not indicate thermodynamic instability. The lattice remains homogeneous, and the growth continues within the mesoscopic 2.5D growth regime, also known as the SK growth mode<sup>36,37,39</sup>. The InSbBi film will be strained because of the lattice mismatch between the substrate and the film. Hence, the thin film will grow in a layer-by-layer fashion until a certain critical thickness, beyond which 3D islands or mounds form through the SK transition. This transition marks a shift from two-dimensional (2D) layer-by-layer growth to 3D mound formation, characteristic of the SK growth mode. The effect of the thickness on the mound formation will be further discussed in Sec. D: *Evolution of the mound morphology with thickness*.

In a strained film, the formation of mounds is energetically favorable, as it reduces the strain energy in the crystal<sup>40</sup>. The mound density is higher in Fig. 2(c) compared to Fig. 2(b) due to the increased incorporation of Bi into the film with higher Bi flux. As Bi incorporation increases, the lattice constant of the InSbBi thin film increases, leading to a greater lattice mismatch between the substrate and the thin film. Consequently, more mounds form to reduce the strain energy of the thin film. As the Bi flux increases to  $3.3 \times 10^{-8}$  Torr, the mound morphology in Fig. 2(c) changes, and droplets and elongated nanostructures aligned along the [110] direction begin to form, as shown in Fig. 2(d). The presence of these droplets and nanostructures indicates non-substitutional Bi incorporation<sup>14</sup>. As the Bi flux further increases to  $5.0 \times 10^{-8}$  Torr, the nanostructure size and the droplet density increase, as shown

in Fig. 2(e). The roughness increases exponentially with increasing Bi flux, as shown in Fig. 2(f), indicating the existence of a threshold Bi flux between  $1.7 \times 10^{-8}$  Torr and  $3.3 \times 10^{-8}$  Torr for obtaining InSbBi surfaces without Bi droplets and nanostructures.

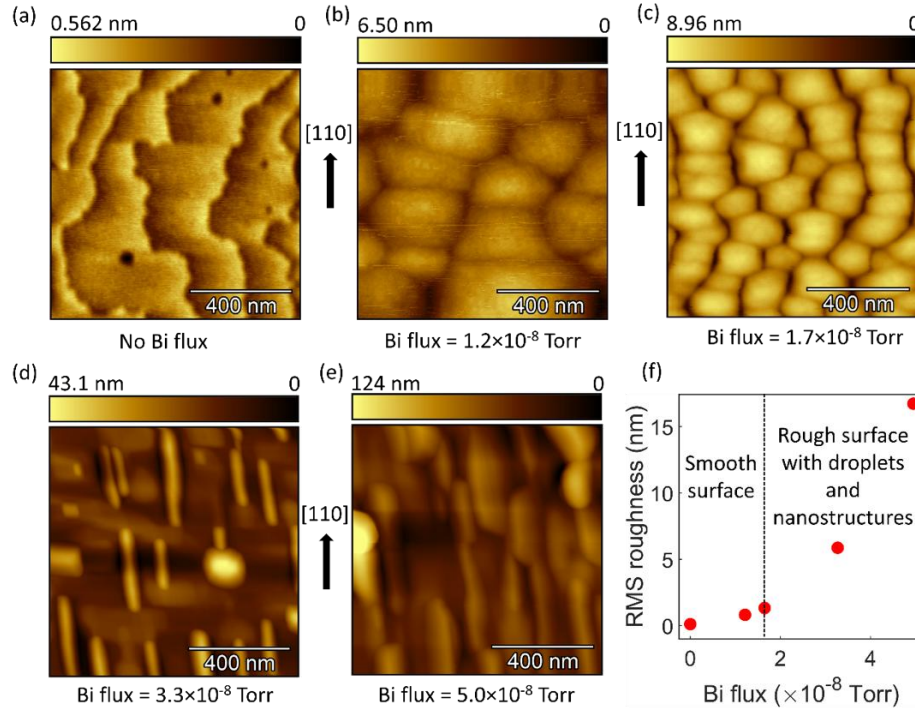


FIG. 2: AFM images showing the evolution of surface morphology with increasing Bi flux. (a) InSb without Bi flux (Bi flux = 0). (b) Bi flux =  $1.2 \times 10^{-8}$  Torr. (c) Bi flux =  $1.7 \times 10^{-8}$  Torr. (d) Bi flux =  $3.3 \times 10^{-8}$  Torr. (e) Bi flux =  $5.0 \times 10^{-8}$  Torr. The black arrow corresponds to the [110] direction in the AFM images. (f) RMS roughness calculated from AFM images.

To assess the crystallography and composition of Bi incorporated into the InSbBi thin films, XRD was conducted on the InSbBi films with Bi flux variation, as shown in Fig. 3(a). An as-is InSb(001) substrate without the InSb buffer layer and the InSbBi film indicated in the blue curve reveals InSb(004) XRD peak at  $56.79^\circ$  with a shoulder peak at  $56.83^\circ$ , corresponding to the  $\text{Sb}_2\text{O}_4(222)$  peak. This  $\text{Sb}_2\text{O}_4(222)$  peak originates from the native oxide layer present on the as-is InSb(001) substrate.

This peak is absent in the other curves because the oxide layer in the as-is InSb(001) substrate is removed through thermal desorption in the presence of Sb. While a new oxide layer will be formed upon exposure to atmosphere after the InSbBi thin film is taken out of the MBE chamber after the completion of the growth, it will be thin and amorphous, lacking the crystalline characteristics required for detectable XRD reflections.

When the Bi flux increases to  $1.2 \times 10^{-8}$  Torr, an InSbBi(004) peak appears, indicating successful Bi incorporation into InSb to form InSbBi. As the Bi flux increases to  $1.7 \times 10^{-8}$  Torr, Bi incorporation further increases, as evidenced by the leftward shift of the InSbBi(400) peak. This shift occurs because Bi incorporation expands the InSbBi lattice constant. When the Bi flux is further increased, the InSbBi peak becomes less prominent (orange curve) and nearly vanishes at  $5.0 \times 10^{-8}$  Torr (red curve). Excess Bi flux prevents substitutional incorporation, leading to Bi accumulation on the surface, forming droplets and nanostructures, as reflected in the AFM results for Bi fluxes above  $3.3 \times 10^{-8}$  Torr, as shown in Figs. 2(d) and 2(e). Hence, a Bi flux of  $1.7 \times 10^{-8}$  Torr yields the best surface quality and epitaxial InSbBi thin film. The Bi incorporation was estimated by fitting dynamical XRD simulations, as shown in Fig. 3(b). Additionally, Laue oscillations are visible when the Bi flux is  $1.7 \times 10^{-8}$  Torr as illustrated by the experimental XRD curve in Fig. 3(b) which indicates the high crystallinity and the uniformity of the InSbBi film and smoothness of the interface between the InSbBi and InSb<sup>41-43</sup>. When the flux is  $1.2 \times 10^{-8}$  Torr, the Bi incorporation is 0.9%. As the Bi flux increases to  $1.7 \times 10^{-8}$  Torr, the Bi incorporation rises to 1.81%. Hence, by increasing the Bi flux up to a certain threshold ( $3.3 \times 10^{-8}$  Torr), the Bi incorporation in the InSbBi film can be tuned.

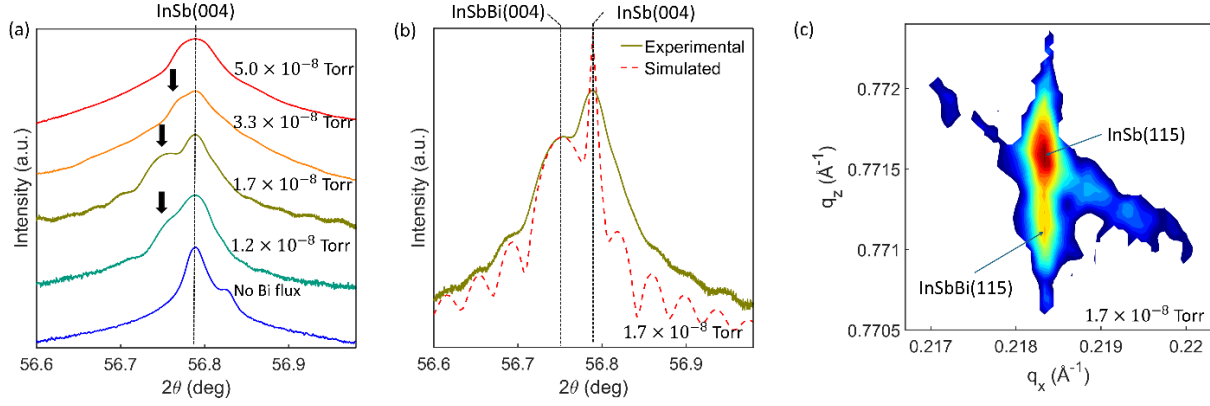


FIG. 3: (a)  $\theta/2\theta$  XRD results of the InSbBi thin films with varying Bi flux from no flux to  $5.0 \times 10^{-8}$  Torr. Black arrows correspond to the InSbBi(004) peaks. (b) Experimental and simulated XRD results for the InSbBi thin film with a Bi flux of  $1.7 \times 10^{-8}$  Torr. (c) The RSM results for the InSbBi thin film with a Bi flux of  $1.7 \times 10^{-8}$  Torr in (b). The first XRD curve in (a) plotted in blue is for the InSb(001) substrate without any InSbBi thin film.

To gain a comprehensive understanding of the strain in InSbBi thin films grown on an InSb(001) substrate, a reciprocal space map (RSM) was performed on the sample grown with a Bi flux of  $1.7 \times 10^{-8}$  Torr, focusing on the (115) reflection, as illustrated in Fig. 3(c). The corresponding XRD data is presented in Fig. 3(b). The presence of strain in the InSbBi thin film is evident from the alignment of the InSbBi(115) peak with the InSb(115) peak along  $q_x$ , indicating that the in-plane lattice parameter of the film matches that of the substrate.

Table 1: Calculation of strain on InSbBi thin films obtained from RSM results.

Out-of-plane lattice constant (XRD) [ $\text{\AA}$ ]	In-plane lattice constant (RSM) [ $\text{\AA}$ ]	Out-of-plane lattice constant (RSM) [ $\text{\AA}$ ]	In-plane strain [%]	Out-of-plane strain [%]	Poisson ratio
6.483	6.477	6.484	0.093	0.015	0.087

The in-plane and out-of-plane strains were quantified using lattice constants extracted from the RSM peaks, as summarized in Table 1. The strain ( $\epsilon$ ) was calculated using the relation  $\epsilon = (a_{\text{strained}} -$

$a_0)/a_0$ , where  $a_{\text{strained}}$  represents either the in-plane or out-of-plane lattice parameter of the strained InSbBi film, and  $a_0$  is the relaxed lattice parameter of InSbBi (6.483 Å). The relaxed lattice constant was calculated from the Vegard's law combined with a bowing coefficient using  $a_{\text{InSbBi}} = xa_{\text{InBi}} + (1 - x)a_{\text{InSb}} + 0.0012x(1 - x)$ , where  $a_{\text{InSbBi}}$ ,  $a_{\text{InBi}}$ ,  $a_{\text{InSb}}$  are the lattice constants of  $\text{InSb}_{1-x}\text{Bi}_x$ , InBi, and InSb, respectively<sup>44</sup>. The Poisson ratio ( $\nu$ ) was determined using the equation

$$\nu = \frac{\epsilon_{\text{out-of-plane}}}{\epsilon_{\text{out-of-plane}} - 2 \times \epsilon_{\text{in-plane}}}$$
, where  $\epsilon_{\text{out-of-plane}}$  and  $\epsilon_{\text{in-plane}}$  represents the out-of-plane and in-plane strains, respectively<sup>45,46</sup>. Here, the out-of-plane strain is multiplied by -1 to account for the tensile in-plane strain of the InSbBi film<sup>45,46</sup>. Notably, the out-of-plane lattice constants derived from both RSM and XRD measurements exhibit close agreement, further validating the strain analysis in the InSbBi thin films.

### C. Change in surface morphology with varying growth temperature

The effect of growth temperature on InSbBi thin film morphology was investigated by varying the temperature from 183°C to 250°C, while maintaining a constant Bi flux of  $1.7 \times 10^{-8}$  Torr. As shown in Fig. 4, significant surface morphology changes occurred with increasing temperature. At a growth temperature of 183°C, the surface shows a rough morphology containing nanostructures and small droplets possibly due to the deposition of Bi on the surface as illustrated in Fig. 4(a). When the growth temperature is increased to 200°C, the InSbBi thin films show the characteristic surface morphology of InSbBi with mounds, as shown in Fig. 4(b). This is the same sample that was discussed earlier in Fig. 2(c). With increasing temperature, the mound morphology of the sample changes. At 217°C, the smaller mounds observed in Fig. 4(b) coalesce to form larger mounds with the height of the mounds being reduced as shown in Fig. 4(c). At 233°C, the onset of the step edges occurs as shown in Fig. 4(d). This indicates a significant diversion from the mound morphology observed for 200°C and 217°C to the step flow growth with step meandering<sup>36,37</sup>. At 250°C, the step flow growth mode is more pronounced as seen in Fig. 4(e). The reason for this behavior is that at elevated temperatures, the

energetic adatoms have high mobility, such that they can migrate across the surface and reach steps for attachment and step formation<sup>47</sup>. The size of the mounds is approximately  $200 \times 200 \text{ nm}^2$  as shown in Fig. 4(f). The 3D topography of the step flow growth is shown in Fig. 4(g). The average height of a step is approximately  $(0.324 \pm 0.001) \text{ nm}$  as illustrated in Fig. 4(h) which is close to the monolayer height of InSb ( $0.324 \text{ nm}$ )<sup>48</sup> which further indicates that the percentage incorporation of Bi is almost zero at  $250^\circ\text{C}$ .

With increasing temperature, the surface gets smoother as shown by the RMS roughness decreasing exponentially as shown in Fig. 4(i) which happens because the surface changes from having a mound morphology to a step flow growth. This can be attributed to the fact that the probability of Bi incorporating into the film to form InSbBi at higher temperatures will decrease owing to the large size of Bi atoms<sup>49</sup>. In fact, this has been observed in GaSbBi and GaAsBi films where Bi has been incorporated to form III-V alloys<sup>49-51</sup>. Raising the growth temperature can promote the surface mobility of Bi atoms and the probability of Bi atoms encountering each other increase. Hence, it can promote droplet formation. Additionally, the bonding energy of Bi-Bi is  $200 \text{ kJ/mol}$  while that of In-Bi is  $153.6 \text{ kJ/mol}$ <sup>52</sup>. Hence, formation of Bi droplets is energetically favorable when compared to the incorporation of Bi into substitutional sites of InSbBi<sup>1</sup>. So, a combination of these two phenomena provides an explanation for the surface roughening at elevated temperatures with the formation of droplets. Hence, it becomes evident that there exists a prominent morphology evolution when the growth temperature is increased from  $200^\circ\text{C}$  to  $250^\circ\text{C}$  indicating that growth temperature plays a vital role in the growth of InSbBi thin films with smooth surface morphology.

To assess the crystallography and the percentage of the Bi incorporated into the InSbBi thin films, XRD was conducted as shown in Fig. 4(j). When the growth temperature is  $200^\circ\text{C}$ , there is a clear InSbBi(400) peak. As the growth temperature increases, the peak shifts right towards the InSb(004) substrate peak. This is to be expected as the Bi incorporation to form InSbBi decreases with the

increase in temperature. The lattice constant decreases with the decrease of Bi percentage in InSbBi which is reflected as a shift in the XRD peak corresponding to InSbBi. This observation agrees well with the AFM RMS roughness data in Fig. S2(e). The XRD plot which corresponds to 250°C which is indicated in red in Fig. 4(f) has no discernible InSbBi(004) peak because the Bi incorporation exponentially decreases at elevated growth temperatures. Hence, at a growth temperature of 250°C, Bi isn't incorporated to form InSbBi. The presence of Laue oscillations in the plots corresponding to 200°C, 217°C, and 233°C in Fig. 5 indicates the high crystallinity and the uniformity of the InSbBi film and smoothness of the interface between the InSbBi and InSb<sup>41-43</sup>. The presence of Laue oscillations in the plot corresponding to 250°C in Fig. 4(f) indicates the high crystallinity and the uniformity of the InSb film when Bi is not incorporated to form InSbBi thin film<sup>41-43</sup>.

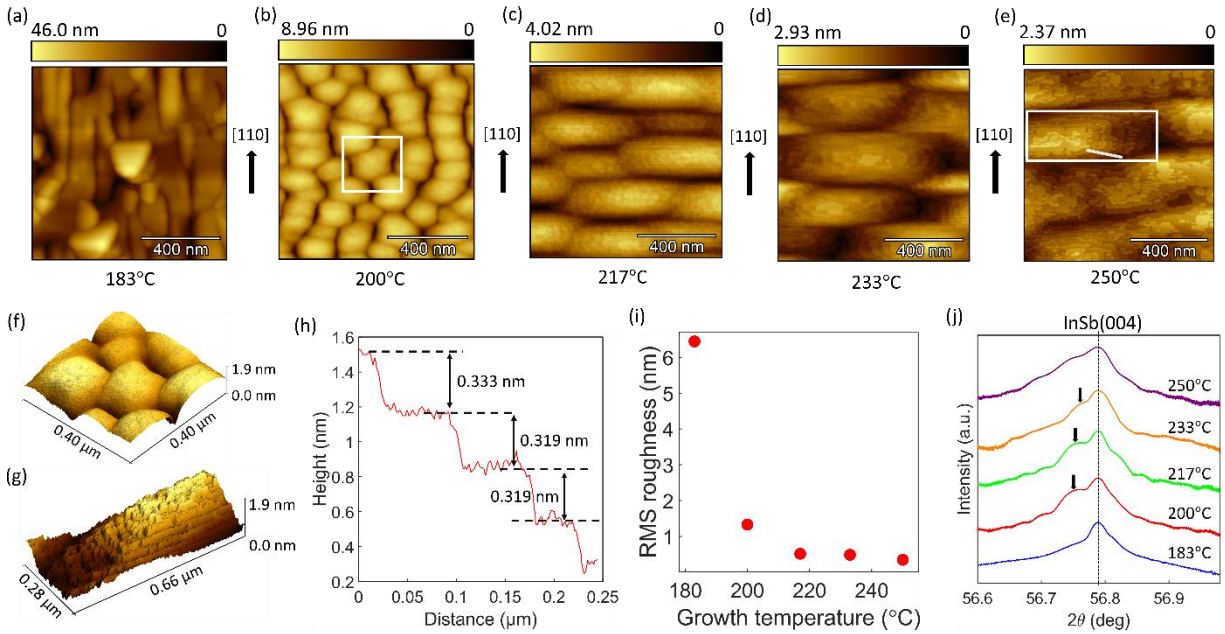


FIG. 4: Change in surface morphology with the growth temperature at a constant Bi flux of  $1.7 \times 10^{-8}$  Torr: (a),(b), (c), (d), and (e)  $1 \times 1 \mu\text{m}^2$  AFM images when the growth temperature = 183°C, 200°C, 217°C, 233°C, and 250°C respectively. The black arrows directed up correspond to the [110] direction of the AFM images. (f) and (g) 3D topographies of the areas indicated in the white rectangles in (b) and (e) representing the mound morphology and the step flow growth respectively. (h) Line profile

of the AFM image in (e) along the white line. (i) RMS roughness obtained from the AFM images. (j)  $\theta/2\theta$  XRD results for the InSbBi thin films corresponding to the samples indicated in the AFM images. The black arrows directed down correspond to the InSbBi(004) peaks.

#### **D. Evolution of the mound morphology with thickness**

The evolution of the mound morphology was studied by systematically increasing the InSbBi film thickness while maintaining the Bi flux at  $1.7 \times 10^{-8}$  Torr and the growth temperature at 200°C (Fig. 4). InSb exhibits a step-edge morphology, as shown in Fig. 5(a). When 20 nm of InSbBi is grown, the step-flow morphology of InSb becomes less prominent, and the onset of mound formation is clearly visible on the terraces. As InSbBi film thickness increases, the small mounds coalesce and increase in size. At film thickness of 150 nm, the peaks of the mounds appear to develop additional smaller mounds, as shown in Fig. 5(c). This occurs because arriving adatoms preferentially nucleate on top of existing mounds, leading to the sequential formation of second-layer nuclei, followed by third-layer nucleation, and so forth. When the film thickness is 300 nm, the mounds appear smoother (Fig. 5(d)). This is the same sample presented in Fig. 2(c) and Fig. 4(b). The primary reason for this smoothing is strain relaxation with increasing thickness. As the film grows, strain gradually dissipates, leading to a reduction in surface instabilities that contribute to roughening. This is further supported by the minimal in-plane and out-of-plane strains observed, as shown in Table 1. As film thickness increases, the RMS roughness also increases (Fig. 5(d)), which is mainly due to the simultaneous increase in the mound height with the film thickness.

XRD scans reveal the crystallographic structure and the composition of the films, as shown in Fig. 5(f). InSbBi(004) peaks are clearly visible, with the peaks shifting towards the InSb(004) peak as the film thickness increases. This shift can be attributed to the film relaxation that occurs with increased thickness, allowing for a reduction in strain and closer alignment with the InSb(004) substrate peak. Specifically, the out-of-plane strains calculated from XRD for the 20 nm and 150 nm InSbBi films are 0.031% and 0.021%, respectively. These values are higher than the out-of-plane strain observed for

the 300 nm sample, as shown in Table 1. The presence of Laue oscillations in the samples containing InSbBi thin films indicates the high crystallinity and the uniformity of the InSbBi thin film<sup>41-43</sup>.

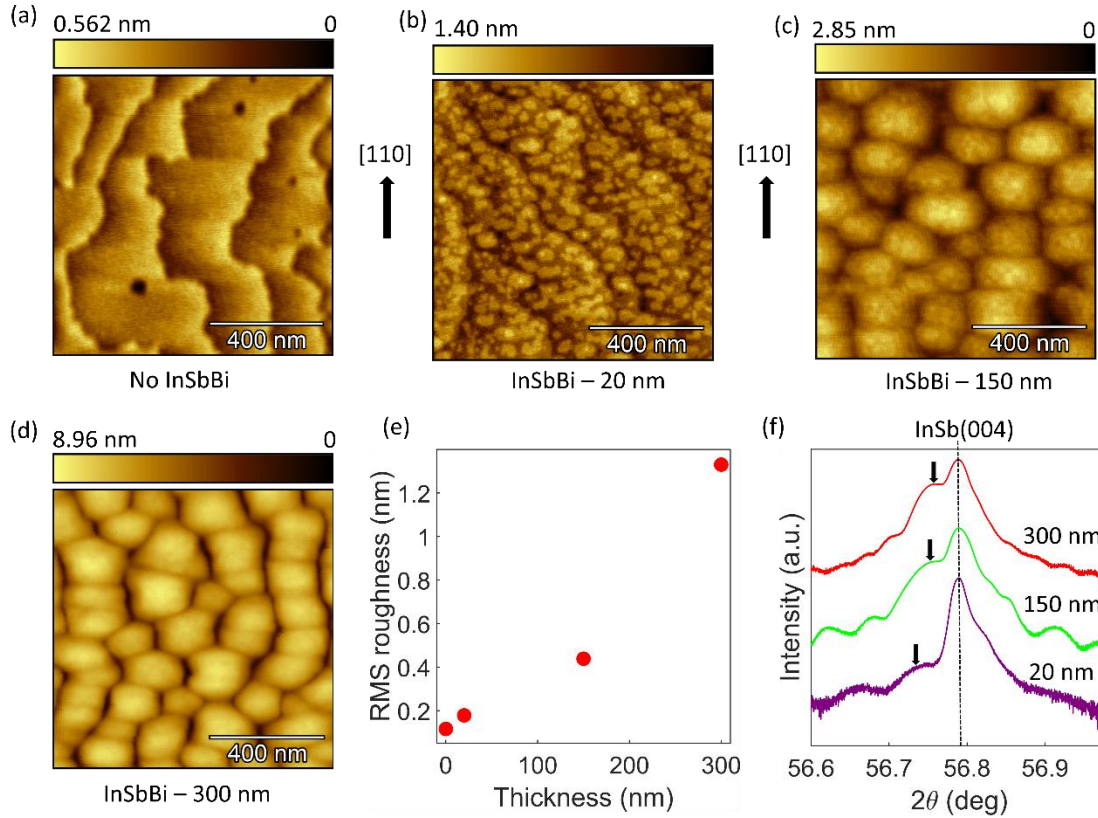


FIG. 5: Change in surface morphology with the thickness at a constant Bi flux of  $1.7 \times 10^{-8}$  Torr and a fixed growth temperature of 200°C. (a), (b), (c), and (d)  $1 \times 1 \mu\text{m}^2$  AFM images when thickness of the InSbBi thin film is 0 nm, 20 nm, 150 nm and 300 nm respectively. (e) RMS roughness calculated from the AFM images. (f)  $\theta/2\theta$  XRD results for the InSbBi thin films corresponding to the samples indicated in the AFM images. The black arrows directed down correspond to the InSbBi(004) peaks.

Hence, it is evident that the Bi incorporation can be tuned by either changing the Bi flux or the growth temperature keeping the other growth parameters constant as shown in Fig. 6(a) and (b). A maximum of 1.81% Bi incorporation was achieved having smooth surface morphology with an RMS roughness  $< 2$  nm.

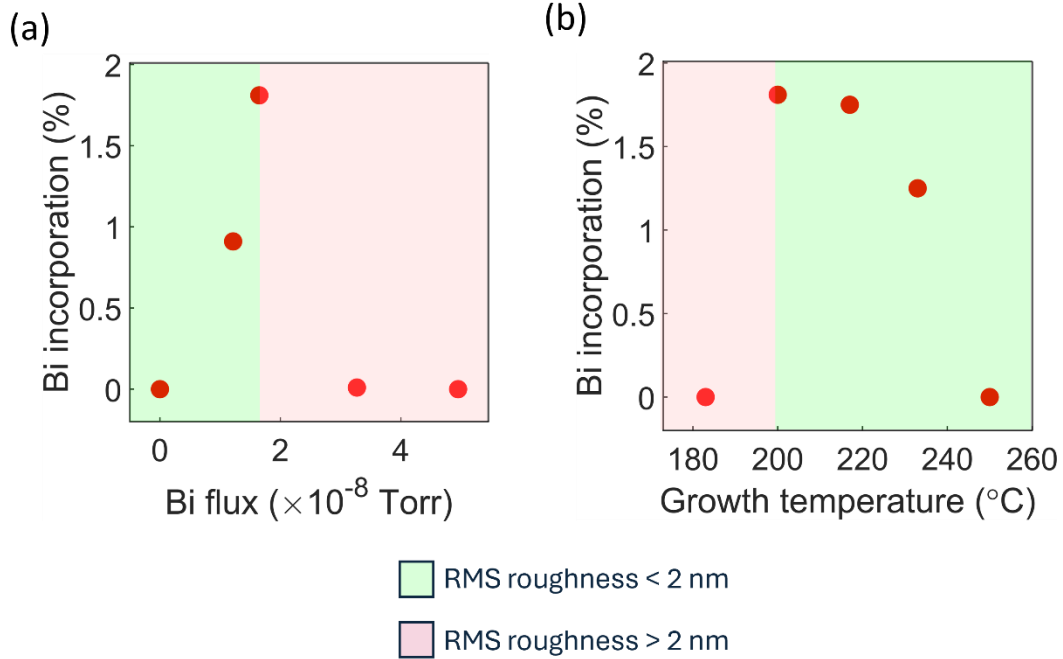


FIG. 6 : Bi incorporation varies with (a) the Bi flux and (b) the growth temperature, respectively. The green and pink regions indicate the growth temperature and the Bi flux window for obtaining samples with smooth (RMS roughness < 2 nm) and rough (RMS roughness > 2 nm) surfaces respectively.

#### IV. CONCLUSION

In summary, we have established a robust methodology for the growth of high-quality InSbBi thin films with Bi incorporation up to 1.81% on InSb(001). Our findings reveal a distinct transition in the growth mode from a mound-dominated morphology to step-flow growth, driven by the interplay between growth parameters and Bi incorporation. Notably, smooth thin films exhibiting mound surface morphology achieve an RMS roughness of <2 nm, as quantified by AFM. The precise Bi incorporation is determined through fitting of simulated and experimental XRD patterns. We demonstrate that achieving atomically smooth films requires maintaining a V/III flux ratio of unity, dynamically calibrated via RHEED analysis. Furthermore, Bi incorporation can be finely tuned by

varying the growth temperature between 200°C and 250°C or adjusting the Bi flux between  $1.2 \times 10^{-8}$  Torr and  $1.7 \times 10^{-8}$  Torr, while keeping other growth parameters constant. These results mark a significant advancement in the growth of high-quality InSbBi thin films, laying the foundation for their integration in the next-generation optoelectronic and quantum device applications.

## ACKNOWLEDGMENTS

This work was supported by the Science Alliance at the University of Tennessee, Knoxville, through the Support for Affiliated Research Teams (StART) program. Structural characterizations were carried out as part of a user project at the Center for Nanophase Materials Sciences, which is a U.S. Department of Energy, Office of Science User Facility at Oak Ridge National Laboratory.

## AUTHOR DECLARATIONS

The authors have no conflicts to disclose.

## DATA AVAILABILITY

The data that supports the findings of this study are available from the corresponding author upon reasonable request.

## REFERENCES

- <sup>1</sup> K.H. Tan, W.K. Loke, S. Wicaksono, and S.F. Yoon, "Growth of droplet-free InSbBi on GaAs substrate," *AIP Adv* **13**(12), (2023).
- <sup>2</sup> W.K. Loke, K.H. Tan, S. Wicaksono, and S.F. Yoon, "Effect of growth temperature and Sb over in flux ratio on the Bi content and the surface morphology of InSbBi grown by molecular beam epitaxy," *Materials Science and Engineering: B* **294**, (2023).
- <sup>3</sup> H. Hassan, S.M. Abdulmuhsin, and A.H. AL-Khursan, "Thallium quantum dot photodetectors," *Opt Quantum Electron* **52**(2), 55 (2020).
- <sup>4</sup> M. van Schilfgaarde, A. Sher, and A.-B. Chen, "InTlSb: An infrared detector material?," *Appl Phys Lett* **62**(16), 1857–1859 (1993).
- <sup>5</sup> K.Y. Ma, Z.M. Fang, D.H. Jaw, R.M. Cohen, G.B. Stringfellow, W.P. Kosar, and D.W. Brown, "Organometallic vapor phase epitaxial growth and characterization of InAsBi and InAsSbBi," *Appl Phys Lett* **55**(23), 2420–2422 (1989).
- <sup>6</sup> I.C. Sandall, F. Bastiman, B. White, R. Richards, D. Mendes, J.P.R. David, and C.H. Tan, "Demonstration of InAsBi photoresponse beyond 3.5  $\mu\text{m}$ ," *Appl Phys Lett* **104**(17), (2014).
- <sup>7</sup> M. Van Schilfgaarde, A.B. Chen, S. Krishnamurthy, and A. Sher, "InTlP - A proposed infrared detector material," *Appl Phys Lett* **65**(21), 2714–2716 (1994).
- <sup>8</sup> M.J. Antonell, C.R. Abernathy, A. Sher, M. Berding, M. Van Schilfgaarde, A. Sanjuro, and K. Wong, *Growth of Tl-Containing III-V Materials by Gas-Source Molecular Beam Epitaxy* (1998).
- <sup>9</sup> M.D. Lange, D.F. Storm, and T. Cole, "Molecular-beam epitaxy of InTlAs," *J Electron Mater* **27**(6), 536–541 (1998).
- <sup>10</sup> R. Bencyton, B. Canut, P. Regreny, M. Gendry, G. Grenet, and G. Hollinger, "A comparative study of GaTlAs, InTlAs and GaInTlAs grown by SSMBE: the detrimental effect of indium," in *16th IPRM. 2004 International Conference on Indium Phosphide and Related Materials, 2004.*, (IEEE, n.d.), pp. 497–500.
- <sup>11</sup> J.J. Lee, J.D. Kim, and M. Razeghi, "Growth and characterization of InSbBi for long wavelength infrared photodetectors," *Appl Phys Lett* **70**(24), 3266–3268 (1997).
- <sup>12</sup> I. Vurgaftman, J.R. Meyer, and L.R. Ram-Mohan, "Band parameters for III–V compound semiconductors and their alloys," *J Appl Phys* **89**(11), 5815–5875 (2001).
- <sup>13</sup> M.K. Rajpalke, W.M. Linhart, K.M. Yu, M. Birkett, J. Alaria, J.J. Bomphrey, S. Sallis, L.F.J. Piper, T.S. Jones, M.J. Ashwin, and T.D. Veal, "Bi-induced band gap reduction in epitaxial InSbBi alloys," *Appl Phys Lett* **105**(21), (2014).
- <sup>14</sup> R.C. White, L.J. Nordin, A.J. Muhowski, D. Wasserman, and S.R. Bank, "Photoluminescence from InSb<sub>1-x</sub>Bi<sub>x</sub> alloys at extended wavelengths on InSb," *Appl Phys Lett* **121**(19), (2022).
- <sup>15</sup> D.P. Samajdar, and S. Dhar, "Influence of Bi-related impurity states on the bandgap and spin–orbit splitting energy of dilute III–V–Bi alloys: InP<sub>1-x</sub>Bi<sub>x</sub>, InAs<sub>1-x</sub>Bi<sub>x</sub>, InSb<sub>1-x</sub>Bi<sub>x</sub> and GaSb<sub>1-x</sub>Bi<sub>x</sub>," *Superlattices Microstruct* **89**, 112–119 (2016).

- <sup>16</sup> Y. Zhang, A. Mascarenhas, and L.W. Wang, "Similar and dissimilar aspects of III-V semiconductors containing Bi versus N," *Phys Rev B Condens Matter Mater Phys* **71**(15), (2005).
- <sup>17</sup> D.J. Chadi, "Spin-orbit splitting in crystalline and compositionally disordered semiconductors," *Phys Rev B* **16**(2), 790–796 (1977).
- <sup>18</sup> B. Fluegel, S. Francoeur, A. Mascarenhas, S. Tixier, E.C. Young, and T. Tiedje, "Giant Spin-Orbit Bowing in GaAs<sub>1-x</sub>Bi<sub>x</sub>," *Phys Rev Lett* **97**(6), 067205 (2006).
- <sup>19</sup> R. Winkler, *Spin—Orbit Coupling Effects in Two-Dimensional Electron and Hole Systems* (Springer Berlin Heidelberg, Berlin, Heidelberg, 2003).
- <sup>20</sup> T. Zhang, H. Liu, F. Gao, G. Xu, K. Wang, X. Zhang, G. Cao, T. Wang, J. Zhang, X. Hu, H.O. Li, and G.P. Guo, "Anisotropic g-Factor and Spin-Orbit Field in a Germanium Hut Wire Double Quantum Dot," *Nano Lett* **21**(9), 3835–3842 (2021).
- <sup>21</sup> Y. Kunihashi, Y. Shinohara, S. Hasegawa, H. Nishinaka, M. Yoshimoto, K. Oguri, H. Gotoh, M. Kohda, J. Nitta, and H. Sanada, "Bismuth induced enhancement of Rashba spin-orbit interaction in GaAsBi/GaAs heterostructures," *Appl Phys Lett* **122**(18), (2023).
- <sup>22</sup> M. Sato, and Y. Ando, "Topological superconductors: a review," *Reports on Progress in Physics* **80**(7), (2016).
- <sup>23</sup> W. Mayer, M.C. Dartailh, J. Yuan, K.S. Wickramasinghe, E. Rossi, and J. Shabani, "Gate controlled anomalous phase shift in Al/InAs Josephson junctions," *Nat Commun* **11**(1), 212 (2020).
- <sup>24</sup> J.D. Sau, R.M. Lutchyn, S. Tewari, and S. Das Sarma, "Generic New Platform for Topological Quantum Computation Using Semiconductor Heterostructures," *Phys Rev Lett* **104**(4), 040502 (2010).
- <sup>25</sup> M. Amundsen, J. Linder, J.W.A. Robinson, I. Žutić, and N. Banerjee, "Colloquium: Spin-orbit effects in superconducting hybrid structures," *Rev Mod Phys* **96**(2), 021003 (2024).
- <sup>26</sup> J. Yoshida, T. Kita, O. Wada, and K. Oe, "Temperature Dependence of GaAs<sub>1-x</sub>Bi<sub>x</sub> Band Gap Studied by Photorefectance Spectroscopy," *Jpn J Appl Phys* **42**(Part 1, No. 2A), 371–374 (2003).
- <sup>27</sup> M. Usman, C.A. Broderick, A. Lindsay, and E.P. O'Reilly, "Tight-binding analysis of the electronic structure of dilute bismide alloys of GaP and GaAs," *Phys Rev B* **84**(24), 245202 (2011).
- <sup>28</sup> S. Francoeur, M.J. Seong, A. Mascarenhas, S. Tixier, M. Adamcyk, and T. Tiedje, "Band gap of GaAs<sub>1-x</sub>Bi<sub>x</sub>, 0<x< 3.6%," *Appl Phys Lett* **82**(22), 3874–3876 (2003).
- <sup>29</sup> Y. Song, S. Wang, I.S. Roy, P. Shi, A. Hallen, and Z. Lai, "Molecular beam epitaxy growth of InSb<sub>1-x</sub>Bi<sub>x</sub> thin films," *J Cryst Growth* **378**, 323–328 (2013).
- <sup>30</sup> K. Oe, S. Ando, and K. Sugiyama, "InSb<sub>1-x</sub>Bi<sub>x</sub> Films Grown by Molecular Beam Epitaxy," *Jpn J Appl Phys* **20**(4), L303 (1981).
- <sup>31</sup> W.K. Liu, and M.B. Santos, "Surface reconstructions of InSb(001) during molecular beam epitaxy," *Surf Sci* **319**(1–2), 172–183 (1994).
- <sup>32</sup> A. Janotti, S.H. Wei, and S.B. Zhang, "Theoretical study of the effects of isovalent coalloying of Bi and N in GaAs," *Phys Rev B Condens Matter Mater Phys* **65**(11), 1–5 (2002).

- <sup>33</sup> P. Laukkanen, M.P.J. Punkkinen, N. Räsänen, M. Ahola-Tuomi, M. Kuzmin, J. Lång, J. Sadowski, J. Adell, R.E. Perälä, M. Ropo, K. Kokko, L. Vitos, B. Johansson, M. Pessa, and I.J. Väyrynen, “Bismuth-stabilized  $c(2 \times 6)$  reconstruction on a InSb(100) substrate: Violation of the electron counting model,” *Phys Rev B Condens Matter Mater Phys* **81**(3), (2010).
- <sup>34</sup> M. Yoshimoto, and K. Oe, “Molecular Beam Epitaxy of GaAsBi and Related Quaternary Alloys,” in *Molecular Beam Epitaxy*, (Elsevier, 2018), pp. 197–209.
- <sup>35</sup> P. Arthur Willoughby, P. Capper, P. Safa Kasap, M.R. Baklanov, M. Green, K. Maex, P. Capper, M. Mauk, M. Jamal Deen, P.K. Basu Nanostructured, S. Waveguides, M. Skorobogatiy, M.T. Taschuk, M.J. Brett, by Katsuaki Sato, and E. Saitoh, *Springer Handbook of Electronic and Photonic Materials* (Springer International Publishing, Cham, 2017).
- <sup>36</sup> O. Pierre-Louis, and C. Misbah, “Out-of-Equilibrium Step Meandering on a Vicinal Surface,” *Phys Rev Lett* **76**(25), 4761–4764 (1996).
- <sup>37</sup> T.P. Menasuta, K.A. Grossklaus, J.H. McElearney, and T.E. Vandervelde, “Bismuth surfactant enhancement of surface morphology and film quality of MBE-grown GaSb(100) thin films over a wide range of growth temperatures,” *Journal of Vacuum Science & Technology A* **42**(3), (2024).
- <sup>38</sup> D. Moldovan, and L. Golubovic, “Interfacial coarsening dynamics in epitaxial growth with slope selection,” *Phys Rev E* **61**(6), 6190–6214 (2000).
- <sup>39</sup> M.D. Johnson, C. Orme, A.W. Hunt, D. Graff, J. Sudijono, L.M. Sander, and B.G. Orr, “Stable and unstable growth in molecular beam epitaxy,” *Phys Rev Lett* **72**(1), 116–119 (1994).
- <sup>40</sup> A. Baskaran, and P. Smereka, “Mechanisms of Stranski-Krastanov growth,” *J Appl Phys* **111**(4), (2012).
- <sup>41</sup> J. Xu, J. Katoch, A.S. Ahmed, I. V. Pinchuk, J.R. Young, E. Johnston-Halperin, J. Pelz, and R.K. Kawakami, “Growth of uniform CaGe<sub>2</sub> films by alternating layer molecular beam epitaxy,” *J Cryst Growth* **460**, 134–138 (2017).
- <sup>42</sup> X. Shu, J. Zhou, L. Liu, W. Lin, C. Zhou, S. Chen, Q. Xie, L. Ren, Y. Xiaojiang, H. Yang, and J. Chen, “Role of Interfacial Orbital Hybridization in Spin-Orbit-Torque Generation in Pt-Based Heterostructures,” *Phys Rev Appl* **14**(5), 054056 (2020).
- <sup>43</sup> A.M. Miller, M. Lemon, M.A. Choffel, S.R. Rich, F. Harvel, and D.C. Johnson, “Extracting information from X-ray diffraction patterns containing Laue oscillations,” *Zeitschrift Für Naturforschung B* **77**(4–5), 313–322 (2022).
- <sup>44</sup> C.-Z. Zhao, and Y.-T. Dai, “Lattice constant, bandgap energy, absorption coefficient and dielectric function of the antimony-rich InBixSb<sub>1-x</sub> alloy using first-principles calculations,” *Journal of Physics and Chemistry of Solids* **196**, 112307 (2025).
- <sup>45</sup> C.K. Edirisinghe, A. Rathore, T. Lee, D. Lee, A.-H. Chen, G. Baucom, E. Hershkovitz, A. Wijesinghe, P. Adhikari, S. Yeom, H.S. Lee, H.-K. Choi, H. Kim, M. Yoon, H. Kim, M. Brahlek, H. Rho, and J.S. Lee, “Controlling structural phases of Sn through lattice engineering,” (2024).
- <sup>46</sup> J. Bharathan, J. Narayan, G. Rozgonyi, and G.E. Bulman, “Poisson Ratio of Epitaxial Germanium Films Grown on Silicon,” *J Electron Mater* **42**(1), 40–46 (2013).

- <sup>47</sup> J.Y. Tsao, "Surface Morphology," in *Materials Fundamentals of Molecular Beam Epitaxy*, (Elsevier, 1993), pp. 201–257.
- <sup>48</sup> M.E. Straumanis, and C.D. Kim, "Lattice Parameters, Thermal Expansion Coefficients, Phase Width, and Perfection of the Structure of GaSb and InSb," *J Appl Phys* **36**(12), 3822–3825 (1965).
- <sup>49</sup> A. Duzik, and J.M. Millunchick, "Surface morphology and Bi incorporation in GaSbBi(As)/GaSb films," *J Cryst Growth* **390**, 5–11 (2014).
- <sup>50</sup> W. Pan, L. Wang, Y. Zhang, W. Lei, and S. Wang, "MBE growth strategy and optimization of GaAsBi quantum well light emitting structure beyond 1.2  $\mu\text{m}$ ," *Appl Phys Lett* **114**(15), (2019).
- <sup>51</sup> M.A. Stevens, K.A. Grossklaus, and T.E. Vandervelde, "Strain stabilization of far from equilibrium GaAsBi films," *J Cryst Growth* **527**, (2019).
- <sup>52</sup> Y.-R. Luo, *Comprehensive Handbook of Chemical Bond Energies* (CRC Press, 2007).